



A computational study of supersonic disk-gap-band parachutes using Large-Eddy Simulation coupled to a structural membrane

K. Karagiozis^a, R. Kamakoti^a, F. Cirak^b, C. Pantano^{a,*}

^a Department of Mechanical Science and Engineering, University of Illinois at Urbana-Champaign, 1206 W. Green St. MC-244, Urbana, IL 61801, USA

^b Department of Engineering, University of Cambridge, Cambridge CB2 1PZ, UK

ARTICLE INFO

Article history:

Received 26 March 2010

Accepted 22 November 2010

Available online 22 December 2010

Keywords:

Compressible flow

Large-eddy simulation

Structural membrane

Fluid–membrane interaction

Turbulence–structure interaction

Supersonic parachute

ABSTRACT

Large-scale fluid–structure interaction simulations of compressible flows over flexible supersonic disk-gap-band parachutes are compared with matching experimental results. We utilize adaptive mesh refinement, large-eddy simulation of compressible flow coupled with a thin-shell structural finite-element model. The simulations are carried out in the regime where large canopy-area oscillations are present, around and above Mach 2, where strong nonlinear coupling between the system of bow shocks, turbulent wake and canopy is observed. Comparisons of drag history and its dependence on Mach number are discussed. Furthermore, it is observed that important dynamical features of this coupled system can only be reproduced when sufficient grid resolution is used. Lack of resolution resulted in incorrect flow-physics prediction and, consequently, incorrect fluid–structure interaction coupling.

© 2010 Elsevier Ltd. All rights reserved.

1. Introduction

Supersonic parachutes have been used as aerodynamic decelerators during entry and descent into low-density atmospheres, e.g., for Mars space exploration missions. Owing to their low mass and high packaging efficiency, they provide a highly efficient mean of deceleration from supersonic to subsonic speeds. The behavior of these parachutes, at supersonic speeds, encompasses complex interdependent phenomena in fluid–structure interaction (FSI) research. It involves bluff and porous body aerodynamics, nonlinear structural dynamics and fully coupled interaction between the compressible fluid flow, with shocks, and the membrane structure undergoing large deformations. As observed in some flight regimes, the inflated parachute undergoes rapid oscillatory deformations which greatly affects the parachutes' structural integrity and drag characteristics. This results from inevitable tight coupling between the parachute structure and the surrounding flow. The complex dynamics observed is related to the oscillatory axial movement of the bow shock upstream of the parachute canopy due to over/under pressurization, the disparity between the tensile and the compressive stiffnesses of the suspension lines connecting the parachute with the capsule (entry vehicle), inflation instabilities due to the imbalance of fluid forces with structural forces, which are aggravated by the very low inertia of the parachute, and contact forces due to the folding of the canopy. The performance of the parachute is a function of Mach number, shape and size of the capsule, distance between the capsule and the parachute, the shape and the size of the canopy, the material properties of the canopy and the cables, and the angle of attack of the capsule (Peterson and Strickland, 1996). These complex systems have been studied experimentally, mostly in the 60's, sponsored by the US Air Force, and later by NASA during the qualification of the Viking mission to Mars. The modified cross, disk-gap-band and modified ring-sail parachutes are a legacy in this era.

* Corresponding author. Tel.: +12172441412.

E-mail address: cpantano@illinois.edu (C. Pantano).

Maynard (1960) studied the aerodynamic characteristics of different types of supersonic decelerators including balloons, drag chutes, paragliders, and parachutes. Johnson (1960) investigated the characteristics of a 6-foot drogue-stabilization ribbon parachute at high altitudes for low-supersonic speeds, concentrating in the canopy-filling time, opening shock and inflated drag characteristics. This work involved both wind-tunnel testing and free-flight experiments. As far as parachute performance is concerned, Mach number and porosity played a major role in wind-tunnel and free-flight testing. A high-frequency (violent) breathing with overinflation was observed for Mach numbers between 1.6 and 3 (Maynard, 1961). Similar studies of supersonic parachutes were performed by Charczenko (1962, 1964), including drag and stability characteristics of ribbon parachutes for flat-roof conical-inlet parachutes for Mach numbers ranging from 2.30 to 4.65. However, as expected, based on results from past experiments, large oscillations were also observed for all types of parachutes under all testing conditions. Houtz (1964) developed a semi-analytical model to account for the isotenoid profile shapes used in the parachute. The isotenoid was first derived by Taylor (1963) and is an axisymmetric surface that carries uniform pressure with only meridional stresses and zero hoop stresses, so that the fluid pressure is mainly carried by the cables. In wind-tunnel tests, it was also observed that, at supersonic speeds, small fabric wrinkles on the parachute surface caused oscillations and subsequently catastrophic failure of the parachute. Heinrich (1966) noticed that the parachute suspension lines play an important role on the overall stability of the parachute. They may trigger and/or enhance flow unsteadiness and hence cause rapid stability loss. Finally, Ross and Nebiker (1966) presented a survey of aerodynamic deceleration systems and summarized experimental and theoretical work up to that date on supersonic parachutes and other inflatable decelerators including information about the structural properties of each decelerator. The research had slowly focused into finding solutions for the large parachute oscillations observed at high Mach numbers for all types of parachutes developed so far. These oscillations were established to be a by-product of the wake developed behind the payload capsule located upstream of the parachute. The parachute performance decreased when the decelerator's bow-shock wave was shifted at or upstream of the wake sonic point and the decelerator trailing critical distance for altering the parachute performance was a function of the Mach number, Reynolds number and the geometry of the payload and parachute (Babish III, 1966; Davenport, 1969). A number of supersonic parachute designs were investigated to enhance their high Mach number performance, including Hyperflo (Nickel and Sims, 1964), Parasonic (Pinnell and Bloetscher, 1966), Ring-sail (Whitlock et al., 1967) and the disk-gap-band (DGB) parachutes (Eckstrom, 1966, 1970; Eckstrom and Preisser, 1967; Lemke, 1967; Mayhue and Bobbitt, 1972). These studies were expanded for applications in the low-density Martian atmosphere for the Viking mission (Bendura and Huckins III, 1968; Gillis and Bendura, 1968; Mikulas and Bohon, 1968; Whitlock and Bendura, 1969; Gillis, 1973; Murrow et al., 1973; Bendura et al., 1974; Moog et al., 1974; Couch, 1975; Silbert, 1983; Silbert and Gilbertson, 1989; Strickland and Macha, 1990; Maydew and Peterson, 1991).

A systematic experimental study on the performance of the drag coefficient of a 10% scale-model of the Viking-type DGB parachute was conducted by Steinberg et al. (1974). The measurements started at Mach 0.6 and it was found that the drag coefficient reached a minimum value at Mach 1.0 and slowly increased afterwards for flows up to Mach 1.4. Further Mach number increase degraded the drag performance. It was noted that a substantial drag coefficient performance increase (up to 20%) was achieved by increasing the suspension/line length ratio from 1.16 to 1.73. Four flight-tests of the Viking DGB supersonic parachute were conducted at Mach number and dynamic pressure conditions corresponding to those for the Viking 1975 mission to Mars (Lundstrom et al., 1974). More recent experimental work includes measurements of opening loads for 18 tests of DGB parachutes of varying geometry and nominal diameters from 43.2 to 50.1 ft (Cruz et al., 2003a) and a study of the effect of specific parachute geometries and fabric permeability (porosity) on drag coefficient and stability (Cruz et al., 2003b).

A study of steady and unsteady axisymmetric inviscid flow over a nonporous cavity showed that when the cavity depth of the concave body exceeds a given limit, a periodic solution was formed in agreement with results from experimental observations (Bastianon, 1968). Early linear stability studies indicated that all vibration frequencies appear to be inversely proportional to the linear dimensions and their ratios can be defined in terms of the canopy mass over the suspension line-mass ratio and the elastic properties of the material (Stevens, 1972). Other computational models of DGB parachutes were developed by Poole (1972) and Nerem and Pake (1973) to investigate numerous effects, including damping on the dynamic pressure, the ratio of maximum vehicle load over maximum canopy drag force, the dynamic load at supersonic conditions, inflation rates and stability. A computational model was developed by Houmard (1973) to predict the dynamic stresses during the inflation of the DGB parachute used in the Viking mission. This model included parachute geometry and predicted pressure distributions and transient deployment loads during inflation employing a nonlinear material model to calculate the stress distribution on the parachute during the opening of the canopy. Other weakly coupled computational FSI models have been developed (Lafarge et al., 1994; Nelsen, 1995; Queen and Raiszadeh, 2002; Taylor et al., 2003). Lingard and Darley (2005) and Lingard et al. (2007) have used fully coupled FSI models using the Arbitrary Lagrangian–Eulerian methodology for simulating a flexible supersonic parachute and discussed the effect of the forebody wake on the drag performance, the effect of Mach number on the drag and flow field and the effect of the trailing distance on the parachute drag coefficient. Barnhardt et al. (2007) investigated the rich dynamics observed for the fully opened DGB supersonic parachutes. The last three papers were able to reproduce the large amplitude oscillations due to over- and under-pressurization of the canopy; this was found to be a significant parameter for the violent dynamics and collapse of the skirt of the DGB parachute at high Mach numbers. Barnhardt et al. (2007) used the detached-eddy simulation (DES) approach to investigate the effect of the time-varying deficit in the capsule wake interacting with the bow shock on the canopy. This unsteadiness in the flow created the over- and under-pressurization at the canopy. Gidzak et al. (2009) presented a fluid–structure interaction model based on DES

methodology. It was found that the intensity and unsteadiness of the wake triggers large-scale surface oscillations of the parachute that remains unstable for times much larger than the time required for flow stabilization.

Sengupta et al. (2008) investigated the performance of a 0.813 m DGB parachute in supersonic flow. The Mach number reached values up to 2.5 and the Reynolds number was 3×10^6 , which is representative of the Mars Science Laboratory (MSL) mission flow conditions. The parachute itself was a 4% scaled down MSL parachute and was attached to a 4% scale Viking-heritage entry vehicle also designed for the same mission. Two different configurations, one unconstrained and the other with constraints allowing translation of the parachute only in a single axis were investigated. In-line load cells and high speed cameras recorded measurements for the unsteady and mean drag coefficients as a function of Mach and Reynolds numbers, supersonic inflation, parachute trim angle, projected area and frequency of area oscillations.

In this paper a new computational fluid dynamics (CFD) study is presented investigating the fluid–structure interaction between a scaled-down version of the MSL DGB parachute and supersonic flow. The computational approach utilizes structured adaptive mesh refinement, large-eddy simulation (LES) and an embedded geometry technique to couple the finite-difference flow solver with the finite-element structural thin-shell and cable solvers.

2. Problem description

The structure considered in this study is shown in Fig. 1. It consists of a capsule (payload) shown on the left-hand side of the figure and a canopy (disk-gap-band parachute) shown on the right-hand side of the figure. The reference coordinate system is centered at the plane of maximum diameter of the capsule and the x coordinate is aligned with the capsule–canopy symmetry line (the mean direction of the flow). In these coordinates, the leftmost edge of the band of the parachute in the relaxed state (without loads) is located at a distance $H = 1.824$ m. The width of the band is $L_B = 10.2$ cm and the width of the gap is $L_G = 10.2$ cm. The capsule–canopy system is connected through a set of suspension lines, or cables, anchored at point A with coordinates $x_A = 35.4$ cm (the cables wrap around the canopy and all their ends meet at A). The 12 cables (corresponding to 24 suspension lines) are sewed with the fabric of the canopy along their contact length. Additionally, four cables have been integrated as radial load carrying members in the band and disk leading and trailing edges. The parachute geometry was provided in the form of a cutting pattern for a gore as shown in Fig. 2 (Reuter et al., 2009).

The deployed canopy geometry has been generated using the cutting pattern and the known deployed canopy diameter. To this end, first the suspension lines have been placed around a hemisphere and subsequently the deployed gore shape between the cables has been generated in accordance with the cutting pattern. The capsule geometry is a scaled version of the Viking mission capsule (70° sphere cone entry vehicle). The main dimensions of the capsule are shown in Fig. 3(a), indicating the diameter $d = 16.96$ cm, width $w = 10.72$ cm and the aeroshell half-angle is 70° . The diameter of the canopy is $D = 55.88$ cm and the diameter of the back hole is $D_o = 9.3$ cm, as shown in Fig. 3(b). In all the cases considered in this study $H/d = 10.75$. Finally, the capsule and point A are fixed in space while the canopy and suspension lines are free to move in response to the fluid dynamical forces acting on the system.

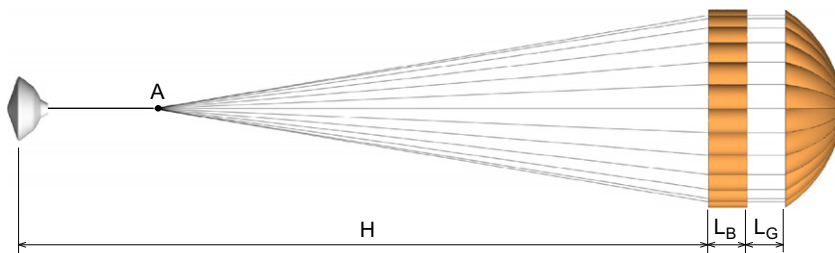


Fig. 1. Overall decelerator configuration.

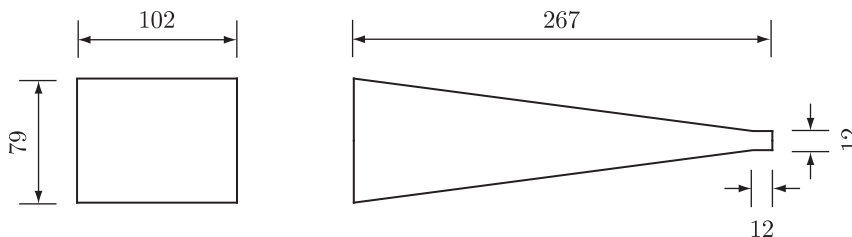


Fig. 2. Cutting pattern for one gore of the band and disc. All dimensions are in mm.

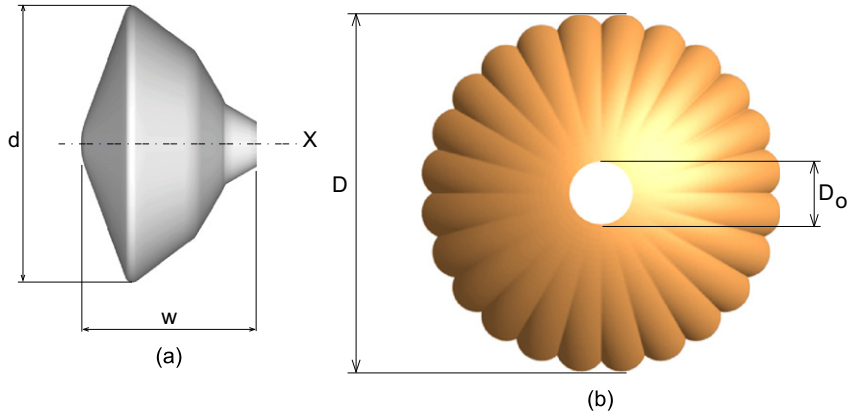


Fig. 3. Viking-type capsule geometry (a) and canopy (b).

3. Governing equations

The flow is governed by the compressible LES equations, i.e., the filtered Navier–Stokes equations, and the fabric is modeled using Kirchhoff–Love thin-shell theory. The fluid governing equations are discretized using a Cartesian adaptive mesh refinement (AMR) approach. Different levels of refinement are used in different regions of the domain depending on resolution needs, according to refinement criteria described below. The structure is discretized using a Lagrangian mesh with subdivision-shell finite elements. In the approach discussed here, the fluid and the solid are coupled loosely. Details of the formulation follow next.

3.1. Fluid

The Favre-filtered, i.e., density weighted, Navier–Stokes equations provide a natural separation of the large scales to be simulated from the small scales to be modeled (Zang et al., 1992). We denote Favre-filtered quantities by

$$\tilde{f} = \frac{\overline{\rho f}}{\bar{\rho}}, \quad (1)$$

where f is an arbitrary field, ρ is the density and the overbar indicates the filtering operation,

$$\bar{f}(\mathbf{x}) = \int G(\mathbf{x}-\mathbf{x}') f(\mathbf{x}') d\mathbf{x}', \quad (2)$$

with convolution kernel G . The filtering procedure combined with some modeling assumptions, e.g., negligible subgrid viscous work and triple correlations, leads to the following LES equations of motion for the density $\bar{\rho}$, momentum $\bar{\rho}\tilde{u}_i$, and total energy \bar{E} ; the dimensional conservation transport equations are:

$$\frac{\partial \bar{\rho}}{\partial t} + \frac{\partial \bar{\rho}\tilde{u}_j}{\partial x_j} = 0, \quad (3)$$

$$\frac{\partial (\bar{\rho}\tilde{u}_i)}{\partial t} + \frac{\partial (\bar{\rho}\tilde{u}_i\tilde{u}_j + \bar{p}\delta_{ij})}{\partial x_j} = \frac{\partial \sigma_{ij}}{\partial x_j} - \frac{\partial \tau_{ij}}{\partial x_j}, \quad (4)$$

$$\frac{\partial \bar{E}}{\partial t} + \frac{\partial (\bar{E} + \bar{p})\tilde{u}_j}{\partial x_j} = \frac{\partial}{\partial x_j} \left(\bar{\kappa} \frac{\partial \bar{T}}{\partial x_j} \right) + \frac{\partial \sigma_{ji}\tilde{u}_i}{\partial x_j} - \frac{\partial q_j^T}{\partial x_j}, \quad (5)$$

where repeated indices denote the summation and the subgrid terms

$$\tau_{ij} = \bar{\rho}(\tilde{u}_i\tilde{u}_j - \tilde{u}_i\tilde{u}_j), \quad (6)$$

$$q_j^T = \bar{\rho}(c_p\tilde{T}\tilde{u}_j - \tilde{c}_p\tilde{T}\tilde{u}_j) \quad (7)$$

denote the subgrid stress tensor and heat transport flux, respectively. The filtered total energy \bar{E} contains the subgrid kinetic energy and is given by

$$\bar{E} = \frac{\bar{p}}{(\gamma-1)} + \frac{1}{2}\bar{\rho}(\tilde{u}_k\tilde{u}_k) + \frac{1}{2}\tau_{kk}, \quad (8)$$

while the filtered pressure, \bar{p} , is determined from the ideal equation of state,

$$\bar{p} = \bar{\rho} R \tilde{T}, \quad (9)$$

where R is the ideal gas constant (2.87085×10^2 J/kg K). This equation together with Eq. (8) defines the Favre-filtered temperature \tilde{T} as a function of \bar{E} , and the subgrid kinetic energy. Formally, the gas is assumed to behave as a single species with the average molecular weight of air. Transport properties are given by

$$\bar{\mu} = 1.73 \times 10^{-5} \text{ kg/m s}, \quad \bar{\kappa} = 2.57 \times 10^{-2} \text{ W/m K}, \quad (10)$$

where $\bar{\mu}$ is the viscosity and $\bar{\kappa}$ is the heat conductivity. The Newtonian stress tensor of the mixture, σ_{ij} , with appropriately filtered quantities is then expressed as

$$\sigma_{ij} = \bar{\mu} \left(\left(\frac{\partial \tilde{u}_i}{\partial x_j} + \frac{\partial \tilde{u}_j}{\partial x_i} \right) - \frac{2}{3} \frac{\partial \tilde{u}_k}{\partial x_k} \delta_{ij} \right), \quad (11)$$

where the usual Stokes approximation is made; no compressibility-related material constitutive parameters are necessary, since this is not a hypersonic flow. Finally, the average specific heat ratio is

$$\tilde{\gamma} = \frac{\tilde{c}_p}{\tilde{c}_v} = 1.4, \quad (12)$$

where the specific heat capacity at constant pressure, \tilde{c}_p , and constant volume, $\tilde{c}_v = \tilde{c}_p - R$, is presumed constant.

The filtering procedure described in Eq. (2) is purely formal. It is not and cannot be performed in LES, unless one has the full direct simulation (or experimental) fields in hand, in which case LES is irrelevant. Here, and henceforth, we identify variables defined formally by Eqs. (1) and (2) with resolved-scale quantities in actual LES. This is strictly a resolved-scale modeling assumption at the level of subgrid quantities described below. For a discussion of this and other conceptual foundations of LES, see Pope (2004).

Closure of the LES equations is completed in the form of a model for the subgrid interaction terms: stress tensor, τ_{ij} , and turbulent temperature flux, q_i^T . This is achieved presently by using the stretched-vortex model, originally developed for incompressible LES (Misra and Pullin, 1997), but extended to compressible flows (Kosovic et al., 2002) and subgrid scalar transport (Pullin, 2000). In this model, the flow within a computational grid cell is assumed to result from an ensemble of straight, nearly axisymmetric vortices aligned with the local resolved-scale strain or vorticity. The resulting subgrid stresses are given by

$$\tau_{ij} = \bar{\rho} \tilde{k} (\delta_{ij} - e_i^v e_j^v), \quad (13)$$

$$q_i^T = -\bar{\rho} \frac{A_c}{2} \tilde{k}^{1/2} (\delta_{ij} - e_i^v e_j^v) \frac{\partial (\tilde{c}_p \tilde{T})}{\partial x_j}, \quad (14)$$

where

$$\tilde{k} = \int_{k_c}^{\infty} E(k) dk \quad (15)$$

is the subgrid energy, \mathbf{e}^v is the unit vector aligned with the subgrid vortex axis, $\nu = \bar{\mu}/\bar{\rho}$ is the kinematic viscosity and $k_c = \pi/\Delta_c$ represents the largest resolved wavenumber by the grid. This subgrid turbulence kinetic energy, \tilde{k} , is estimated by assuming a spiral vortex of the Lundgren (1982) form, whose energy (velocity) spectrum for the subgrid motion is given by

$$E(k) = K_0 \varepsilon^{2/3} k^{-5/3} \exp[-2k^2 \nu / (3|\tilde{a}|)], \quad (16)$$

where K_0 is the Kolmogorov prefactor, ε is the local cell averaged dissipation (resolved flow plus subgrid scale) and $\tilde{a} = \tilde{S}_{ij} e_i^v e_j^v$ is the axial strain along the subgrid vortex axis and

$$\tilde{S}_{ij} = \frac{1}{2} \left(\frac{\partial \tilde{u}_i}{\partial x_j} + \frac{\partial \tilde{u}_j}{\partial x_i} \right) \quad (17)$$

denotes the resolved rate of strain tensor.

To complete the model, the group prefactor $K_0 \varepsilon^{2/3}$ must be calculated for each cell from the resolved flow. This is done by a structure function matching (Lesieur and Metais, 1996; Pullin, 2000; Voelkl et al., 2000). Essentially the second-order velocity structure function $\mathcal{F}_2(\Delta)$ when averaged over the surface of a sphere of radius Δ gives

$$\overline{\mathcal{F}_2(\Delta)} = \frac{4}{\Delta} \int_0^\pi E(s/\Delta) \left(1 - \frac{\sin s}{s} \right) ds. \quad (18)$$

The spectra, Eq. (16), and the assumption that the exponential can be ignored when evaluating at the separation scale Δ gives the group prefactor as

$$K_0 \varepsilon^{2/3} = \frac{\overline{\mathcal{F}_2(\Delta)}}{\Delta^{2/3} \bar{A}}, \quad (19)$$

where $A = 4 \int_0^\pi s^{-5/3} (1 - s^{-1} \sin s) ds \approx 1.90695$. In practice, Δ and Δ_c are taken to be the grid spacing, $(\Delta x \Delta y \Delta z)^{1/3}$, and the spherical average of the structure function is computed as a local estimate using a six-point stencil on the resolved scales

$$\overline{\mathcal{F}_2}(\Delta) = \frac{1}{6} \sum_{j=1}^3 ((\delta \tilde{u}_1^+)^2 + (\delta \tilde{u}_2^+)^2 + (\delta \tilde{u}_3^+)^2 + (\delta \tilde{u}_1^-)^2 + (\delta \tilde{u}_2^-)^2 + (\delta \tilde{u}_3^-)^2), \quad (20)$$

where $\delta \tilde{u}_i^\pm = \tilde{u}_i(\mathbf{x}_0 \pm \mathbf{e}_j \Delta) - \tilde{u}_i(\mathbf{x}_0)$ denotes the i th velocity component difference in the unitary direction \mathbf{e}_j at the point \mathbf{x}_0 .

This subgrid model is based on subgrid elements in the form of spiral-vortices that are local approximate solutions of the Navier–Stokes equations (Lundgren, 1982). In flows where shock–turbulence interaction is important, turbulence passing through shocks is amplified, in an anisotropic way, by baroclinic vorticity production. In the present model, there is no explicit subgrid model representation of this mechanism but when appropriate resolution is used (a premise of LES), most of the turbulence energy spectrum is well resolved and the subgrid contributions are presumed small. Therefore, it is expected that the shock–turbulence interaction modeling uncertainties will be small.

3.2. Thin-shell structure

The canopy of the decelerator is modeled as a thin-shell structure with membrane and bending stiffness. It is clear that the membrane stiffness is significantly larger than the bending stiffness due to the large radius to thickness ratio of the canopy structure. The bending stiffness, however, cannot be neglected, as it determines the intensity and distribution of wrinkling. It is well known that a surface with zero bending stiffness can develop an infinite number of wrinkles of vanishing amplitude under compressive stresses (Pipkin, 1994). From a computational viewpoint, although the inclusion of the small bending stiffness leads to a finite number of wrinkles, the size of the finite elements used has to be chosen, so that they are smaller than the wrinkling wave length. This requirement may lead to impractically large number of elements in large-scale membrane structures. To alleviate this problem, membrane finite elements based on the tension-field theory can be used. The key idea of the tension-field theory, as proposed by Wagner (1929), is to entirely neglect the bending stiffness and the compressive stresses in the membrane (see, e.g., Mosler and Cirak, 2009 for more details). Although tension-field theory can predict the stress state in the structure it cannot reproduce its detailed deformation state usually consisting of an intricate network of cascading wrinkles. More specifically, if tension-field theory is used, there is no wrinkling or, in other terms, no small scale features are present in the computed deflected shape of the membrane. However, it is believed that such fine scale features are crucial for the fluid dynamics at the fluid–structure interface. Therefore, in the present computations a thin-shell model has been used although the used element sizes are too large for resolving all the wrinkles present in the physical model.

The Kirchhoff–Love theory does not consider the out-of-plane shear deformations of the shell and is particularly well suited for modeling thin and extremely thin shell structures. Further details can be found elsewhere (Simo and Fox, 1989; Cirak et al., 2000; Cirak and Ortiz, 2001). Any configuration of the shell is assumed to be defined as

$$\boldsymbol{\varphi} = \mathbf{x} + \xi \mathbf{n} \quad \text{with} \quad -\frac{t}{2} \leq \xi \leq \frac{t}{2}, \quad (21)$$

where $\boldsymbol{\varphi}$ is the position vector of a material point within the shell volume, \mathbf{x} is the position vector of a material point on the mid-surface, Ω , \mathbf{n} is the unit normal to the mid-surface and t is the thickness of the shell. A Lagrangian description is used and quantities with a bar denote reference configuration variables, and quantities without a bar denote current configuration variables. The equilibrium equation of the shell in the weak form can be written as

$$G_{\text{dyn}} + G_{\text{int}} - G_{\text{ext}} = 0, \quad (22)$$

where the first term is the contribution of the inertial forces

$$G_{\text{dyn}} = \int_{\Omega} \rho_s \ddot{\mathbf{x}} \delta \mathbf{x} \, d\bar{\Omega}, \quad (23)$$

with ρ_s denoting the mass density of the surface, $\ddot{\mathbf{x}}$ the acceleration of the mid-surface, and $\delta \mathbf{x}$ are the virtual deformations (or, in other terms, test functions). The integration domain $\bar{\Omega}$ is the shell mid-surface in the reference (i.e., unloaded) configuration. The inertia terms associated with the rotation of the shell normal have been neglected as they are very small for thin shells. Further, the virtual work of the internal forces can be written as consisting of a membrane and a bending part

$$G_{\text{int}} = \int_{\bar{\Omega}} \mathbf{N} \delta \boldsymbol{\alpha} \, d\bar{\Omega} + \int_{\bar{\Omega}} \mathbf{M} \delta \boldsymbol{\beta} \, d\bar{\Omega}, \quad (24)$$

where \mathbf{N} is the stress resultant tensor and $\boldsymbol{\alpha}$ is the conjugate membrane strain tensor. Similarly, \mathbf{M} is the moment resultant tensor and $\boldsymbol{\beta}$ is the respective conjugate bending strain tensor. The strain tensor $\boldsymbol{\alpha}$ depends on the first-order derivatives and the strain tensor $\boldsymbol{\beta}$ on the second-order derivatives of the reference and deformed shell mid-surface $\bar{\mathbf{x}}$ and \mathbf{x} , respectively.

In the presented computations the external virtual work is due to instationary fluid pressure loading

$$G_{\text{ext}} = \int_{\bar{\Omega}} p \mathbf{n} \delta \mathbf{x} \, d\bar{\Omega}, \quad (25)$$

where p is the scalar fluid pressure, which may vary in space and time. The pressure loading is always in the direction of the shell normal and orthogonal to the mid-surface.

The conforming finite-element discretization of the internal virtual work, Eq. (24), requires shape functions with square integrable second-order derivatives (because of the second-order derivatives present in β). In the present work, smooth subdivision surfaces, as introduced in Cirak et al. (2000), have been used as shape functions. Subdivision surfaces can be understood as the generalization of splines to unstructured meshes and are identical to splines on structured meshes. On a structured quadrilateral surface mesh each node is shared by four elements, and on a structured triangular mesh each node is shared by six triangles. Insertion of the subdivision shape functions into Eqs. (23)–(25) and numerical integration with one quadrature point per finite element leads to the semi-discrete equations of motion:

$$\mathbf{M}\ddot{\mathbf{x}}_h + \mathbf{f}_{\text{int}}(\mathbf{x}_h) - \mathbf{f}_{\text{ext}}(\mathbf{x}_h, t) = 0, \quad (26)$$

where $\ddot{\mathbf{x}}_h$ and \mathbf{x}_h are the acceleration and position vectors of the finite-element nodes, respectively and \mathbf{M} is the mass matrix, \mathbf{f}_{int} is the internal force vector and \mathbf{f}_{ext} is the external force vector. An essential feature of the finite-element concept used is that the nodal positions (\mathbf{x}_h) and accelerations ($\ddot{\mathbf{x}}_h$) of the mid-surface are the only degrees of freedom. The semi-discrete equations of motion, Eq. (26), are integrated in time with the explicit Newmark scheme using a lumped mass matrix approximation. Furthermore, in the simulations discussed below, the critical time step size of the shell solver is about a factor of ≈ 10 smaller than that of the fluid solver. A balanced simulation cost is achieved by exchanging pressure and structure position once every 10 shell solver time steps (sub-cycling).

3.3. Boundary conditions and coupling

The interaction between the fluid and the structure is modeled only around the interface separating the two media, using a loosely coupled approach. The CFD and FEA models interact in computational terms only in a thin region around the interface boundary using a temporal splitting method. This interaction is modeled using a variant of the ghost-fluid method (GFM) (Fedkiw et al., 1999). In this technique, the fluid state in the cells covered (overlapped) by the solid are reconstructed with values that satisfy the desired boundary conditions at the location of the interface between solid and fluid. These reconstructed cells are referred to as ghost cells and we use a level set technique (Cirak et al., 2006; Deiterding et al., 2006) to represent the solid boundary in the Cartesian fluid solver. The idea behind the GFM technique is sketched in Fig. 4. First, the solid geometry is converted into a level set (a distance function). Second, the computational cells are divided into two groups, those with positive distance function are labeled fluid cells (lower left-hand side) and those with negative distance function are labeled ghost cells (upper right-hand side). The vector of state of the flow at the ghost cells, blue points in Fig. 4, is obtained from the state in the mirrored fluid side; the closest specular location to the ghost cell with respect to the boundary (orange points). Interpolation is used to reconstruct the state at the mirrored points since they do not coincide, in general, with the coordinates of the center of the fluid cells. In the present Cartesian embedded geometry methodology, the fluid feels a thin-shell represented by the mid-surface Γ , of thickness $\tau\Delta$, where $\Delta = (\Delta x \Delta y \Delta z)^{1/3}$ and $\tau \approx 1.75$ in the present simulations. This regularizes the thin shell to a thickness that can be resolved by the Cartesian discretization of the fluid equations. Fig. 5 shows a two-dimensional cut through the center of the three-dimensional domain at one instant highlighting the region around the canopy (pressure shown as isocontour levels) with the zero level set separating the fluid from the ghost cells shown as a closed black curve.

The coupling force on each shell finite element is evaluated as the difference between the fluid pressure on its top surface \bar{p}^+ and the fluid pressure on its bottom surfaces \bar{p}^- ,

$$\Delta p = \bar{p}^+ - \bar{p}^-. \quad (27)$$

It is assumed that the shell surface is oriented, so that a unique definition of a top and a bottom surface is possible. The quantity in the right-hand side of Eq. (27) is also known as the transmural pressure. Note that Eq. (27) neglects the usually small subgrid pressure forces that are not resolved by the subgrid closure used in the present LES. Incorporating a more

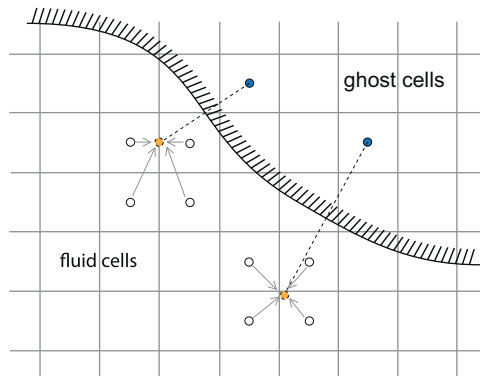


Fig. 4. Sketch indicating the idea behind the ghost-fluid method.

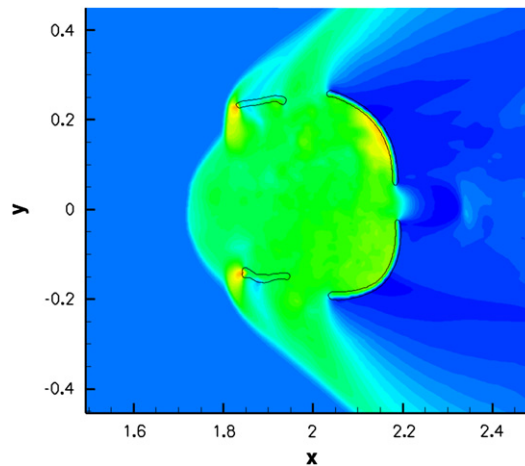


Fig. 5. Ghost region around a narrow band of the canopy at one instant in a simulation (cut through the center of the domain).

accurate linear momentum balance at the interface involves accounting for resolved viscous stresses on the turbulent (attached and detached) boundary layers as well as the coupling of the subgrid stresses to the subgrid wrinkling of the membrane. Unfortunately, modeling these features is beyond the present study, since no established approaches have been developed for subgrid turbulent–wrinkling interactions at such high Reynolds numbers.

Instead, the solid boundaries satisfy the slip boundary condition, essentially an inviscid approximation, while the pressure and density satisfy the zero normal gradient condition; the appropriate limit of perfectly reflective wall-boundary condition in the inviscid approximation (Whitham, 1999). Note that LES is active in the wake of the capsule and canopy, which is important for the description of the fluid–structure interaction of this particular parachute, but the assumed slip boundary condition essentially eliminates the boundary layers around the deformable and rigid structures. The assumption of slip boundaries in general flows is not always sufficiently accurate; certainly not in flows around streamlined objects. In our case, the separation of the boundary layers, formation of the recirculation region and wake behind the capsule and the canopy, are rather well defined due to the blunt geometry of the structures. To a reasonable degree of approximation, the separation occurs near the location of maximum diameter of the structure in question. Moreover, most of the drag is determined by the pressure distribution around the object (form drag). This was verified in a previous study using a rigid capsule–canopy system (Sengupta et al., 2009b), where our methodology was compared with an unstructured mesh technique with wall normal resolution of the turbulent boundary layers using DES. In those simulations, our drag had an error between 3% and 6% at Mach 2 and 2.5, respectively. We expect that this reasonable agreement, in our opinion, will not materialize if the capsule is placed at an angle of attack (AOA) with respect to the free stream, as will most likely happen in real flying conditions (as opposed to the present results that match an experimental arrangement). In this case, there is usually flow separation in the windward side of the capsule which alters the flow around and behind the capsule. The far away wake takes an elliptical cross-section (as opposed to circular for zero AOA). An improvement over our current approach consists of solving the boundary layer approximation of the Reynolds averaged Navier–Stokes (RANS) equations near the structure, preferably using a local frame of reference attached to the finite-element representation of the structure, and couple the resulting stresses to the LES outside the boundary layer. An alternative approach is to use a more sophisticated boundary layer closure (Geurts, 2008). This should improve the modeling of the flow around the rigid structure and possibly the flow around the flexible structure, if the technical challenges associated with incorporating the time-dependent nature of the surface are somehow resolved. Some of these improvements are being pursued as part of future research. Finally, note that even if these improvements were incorporated, one still faces the hard problem of accurately predicting the location of transition from laminar to turbulent flow (which is not a solved problem in general, even for flow over non-deformable structures). Moreover, it does not appear that any of these details could play an important, or dramatic, role in the nature of the fluid–structure interaction considered presently.

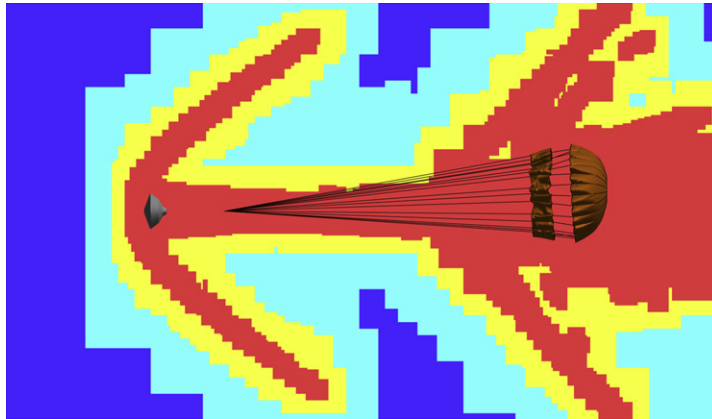
4. Parameters of the simulations

Three simulations were conducted to investigate the effect of Mach number, $M = u_\infty/c_\infty$, and dynamic pressure, $q = \frac{1}{2}\rho_\infty u_\infty^2$, where u_∞ , ρ_∞ and c_∞ denote the free-stream velocity, density and speed of sound, respectively. The Reynolds number is defined using the capsule diameter, according to $Re = \rho_\infty u_\infty d/\mu_\infty$, where μ_∞ denotes the dynamic viscosity at the conditions of the flow upstream. One additional simulation was conducted at lower resolution to assess the effect of grid size on the results. Table 1 lists the fluid mechanical parameters of these simulations. The structural parameters of the fabric are: Young's modulus $E = 878$ MPa, Poisson's ratio $\nu = 0.33$, thickness of the fabric $h = 6.35 \cdot 10^{-2}$ mm and density $\rho_s = 614$ kg/m³. The properties of the cables are: diameter $\phi = 0.495$ mm, elastic modulus $E_c = 43$ GPa and linear density $\rho_c = 8.27 \cdot 10^{-4}$ kg/m. These structural and flow parameters match those in the experiments of Sengupta et al. (2009c). Several experiments were carried out at different Mach

Table 1

Flow parameters of the simulations.

Case	M	Re	q (Pa)	u_∞ (m/s)	Δ_{\min} (mm)
A'	1.96	122,143	4202.5	674.9	7.8
A	1.96	122,143	4202.5	674.9	3.9
B	1.96	162,424	4202.5	507.5	3.9
C	2.48	651,646	19,291	580.7	3.9

**Fig. 6.** Example of mesh distribution at one instant in simulation A (cut through the center of the domain). Coarse through fine meshes are denoted by rectangular patches shown in blue, cyan, yellow to red, respectively.

numbers, different dynamic pressures and with constrained and unconstrained canopies. In this paper, we consider the unconstrained parachutes for Mach 2.0 at the low dynamic pressure and Mach 2.5 at the high dynamic pressure case. The flexible canopy was discretized using triangular finite elements involving 11 688 elements for Case A' and 92 016 elements for Cases A to C.

The computational domain was $[-3,5] \times [-1,1] \times [-1,1]$ (all lengthscales in meters), with the capsule centered at the origin. The coarse mesh resolution of the base level of the AMR, L_0 , is $\Delta x = \Delta y = \Delta z = 1/32$ m. Case A' used two additional levels of refinement (total three levels) and Cases A, B and C used three additional levels of refinement (total four levels). The refinement ratio between level L_i and L_{i+1} is 2 for all levels and in all directions. The grid density was controlled according to the following dynamic refinement criteria: the regions around all structures, rigid capsule and deforming canopy, were refined to the finest resolution; the regions covered by the turbulent wakes, behind the capsule and canopy, were also refined to the finest resolution. The latter relies on the subgrid-scale turbulence kinetic energy, k , estimate provided by the subgrid-scale model, Eq. (15). The shocks were detected dynamically by a shock-detection algorithm that involves determining the Rankine–Hugoniot jump conditions at all cells of the computational domain (at all levels) (Lombardini, 2008). Those cells that contain a shock, according to the jump conditions, are flagged for refinement at the finest resolution possible. These criteria are applied every four time steps of the coarse AMR mesh. This interval was found to be sufficient, since there are sufficient guard cells around those cells that are strictly flagged for refinement. Fig. 6 shows the grid levels at the x – y plane through the center of the domain of Case A at one instant. The different refinement levels are indicated with different colors: blue, cyan, yellow and red, denoting levels L_0 to L_3 , respectively. These refinement criteria were selected to maximize the mesh utilization in the regions of the flow where the largest gradients, e.g., shocks, complex geometry and turbulence are present, while keeping the computational costs as low as possible. The interaction of the suspension lines with the flow was ignored in these simulations. The diameter of these cables is too small to be resolved with current computational resources. The total number of grid cells in the simulations varies with time in each case but ranges approximately around 12 and 50 million for Case A' and Cases A to D, respectively. The simulations were run on a SGI Altix 3700 System at the Supercomputer and Visualization Facility of the Jet Propulsion Laboratory. Each simulation utilized 100 processors (96 assigned to the fluid and 4 to the structure) and required approximately 4 months to complete on an almost continuous basis.

5. Results

The structure is placed in a supersonic flow going from the left to the right of Fig. 1. Two bow shocks develop, one ahead of the capsule and one ahead of the canopy. The high Reynolds number of the present application results in the generation of a turbulent wake behind the capsule. This wake interacts with the bow shock ahead of the canopy and provides the main source of fluid dynamical unsteadiness. An analogous behavior is observed during the interaction of vortical structures with subsonic parachutes (Johari and Levshin, 2009). The intensity of the turbulence carried by the wake is amplified as it is

ingested by the canopy bow shock (due to turbulence–shock interaction). The amplified turbulence fluctuations lead to amplified pressure fluctuations. These, coupled with the structural dynamics of the canopy, induce large inhomogeneous pressure variations, leading to large canopy area oscillations in the Mach number range from 1.5 to 2.5. This is a type of oscillatory breathing phenomenon that produces large drag variations and substantial stress fluctuations in the structure. This affects negatively the ability of the supersonic parachute to act as an effective decelerating device. In the present study, we consider cases in the Mach 2–2.5 range.

Fig. 7 shows a composite view of Case C at $t=60$ ms. In this view, the rigid capsule is located at the bottom left-hand side of the figure and the canopy is approximately in the center of the domain. The canopy is superimposed over Mach number isolevels at the plane through the center of the domain at this particular instant. This composite view is a compromise among other visualization possibilities of the three-dimensional flow and it highlights the shape of the canopy over more detailed flow features rendering shown in the next figure.

The compressible flow around the supersonic parachute can be decomposed into a number of canonical regions, as shown in Fig. 8. Here, the capsule, canopy and suspension lines as well as color isocontour levels of the streamwise velocity, \tilde{u} , and isolines of pressure (in black) for Case A at $t=57.5$ ms are shown in the central plane of the computational domain. In this figure, we observe the two bow shocks, BS_1 and BS_2 , ahead of the capsule and the canopy, respectively. These shocks are responsible for adjusting the supersonic flow conditions upstream to the solid boundaries of the rigid capsule and flexible canopy. A quite stable narrow turbulent wake develops behind the capsule, TW_1 , while a more irregular turbulent wake, TW_2 , is present behind the canopy. The latter experiences large variability due to the deformation of the canopy. The detached flow

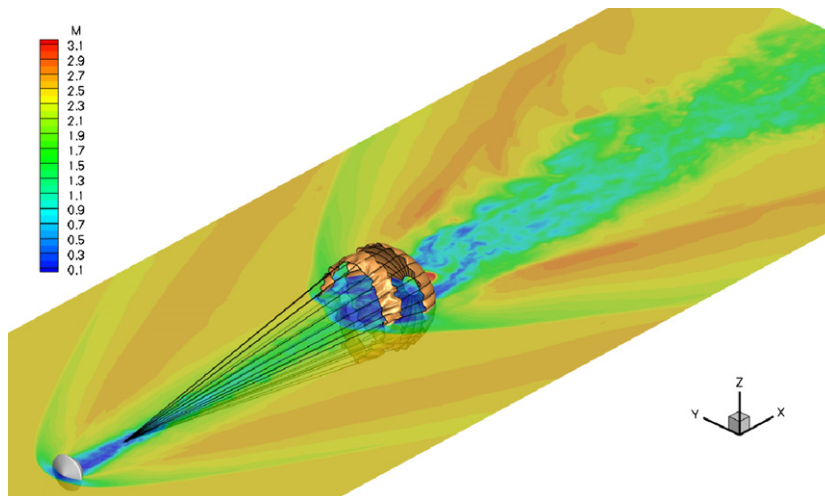


Fig. 7. Three-dimensional composite rendering of the Mach number at the center plane, including capsule, canopy and suspension lines for Case C at $t=60$ ms.

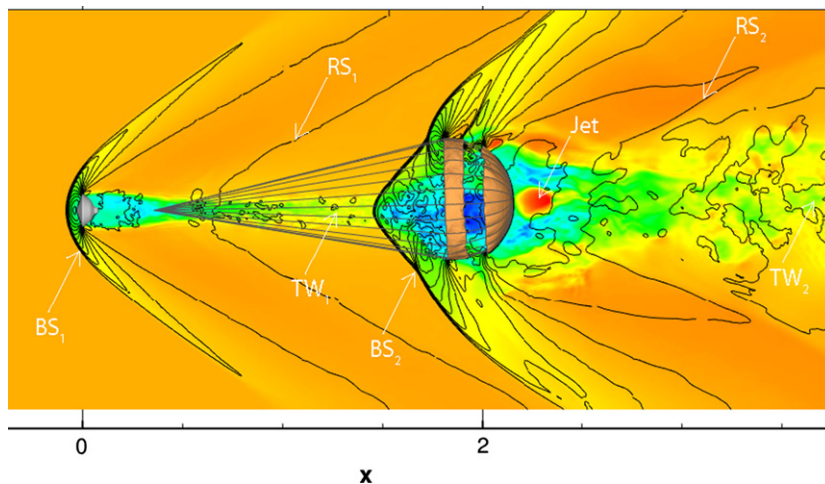


Fig. 8. General flow features around the interacting surfaces. Isocontours indicate streamwise velocity and isolines indicate pressure for Case A at one instant.

in the region immediately behind the capsule and the canopy is rectified by two recompression shocks, RS_1 and RS_2 , that reconcile the oblique flow direction just behind the blunt structures with the free-stream direction. In this figure, we also observe part of the supersonic jet leaving the hole in the back of the canopy (the center of the canopy is slightly off the center plane at this instant, and therefore, the figure does not show a cut through the center of the jet). As pointed out in the introduction, the main source of instabilities originate in the shock–turbulence interaction between TW_1 and BS_2 (Ross and Nebiker, 1966). The bow shock is disturbed by the unstationarity and irregularities of the wake (since the wake is not instantaneously cylindrical) and its momentum and pressure fluctuations are amplified as the flow traverses the bow shock (turbulence ingestion by the shock). The resulting pressure fluctuations are now larger and they enhance transmural forces across the canopy. These, in turn, induce large amplitude deformations of the canopy which feedback into the bow-shock location inducing large oscillations of BS_2 that further reinforce unsteady pressure forces in the region of the canopy, where the compressed flow resides. It is thought that this cycle maintains and generates the breathing phenomena observed in this supersonic parachute. Note that a flexible canopy is not required for the bow shock to develop unstationary (irregular) motion; this is present regardless of the deformable structure (Barnhardt et al., 2007).

5.1. Canopy dynamics

Fig. 9 shows the evolution, with time, of the projected frontal area of the canopy for all cases normalized by the initial area $S_0 = \pi D^2/4 = 0.2452 \text{ m}^2$. These curves relay a purely geometrical interpretation of the behavior of the canopy, and consequently the drag, to be discussed below, and help quantify the magnitude of the breathing phenomena inherent in these supersonic parachutes. It is observed that the initial transient of all the simulations, except for Case A', is completed and the canopy enter into the breathing cycle mode in approximately 25 ms. The figure shows two, well defined, complete cycles for Cases A through C. Case A' (at the lower resolution) exhibits an anomalous behavior. Note that the only difference between Cases A' and A is the additional level of resolution in the latter simulation (mesh twice as fine). Therefore, it appears that resolution is a factor at play in Case A'; to be discussed in Section 5.3.

Fig. 10 indicates five instants in the last cycle of simulation A, labeled α to δ , that will be scrutinized in more detail. These instants correspond to the typical phases the canopy experiences, starting with the point of maximum inflation, α , average inflation, β and δ , and minimum inflation, γ . Note that the area varies by more than 60% between peaks and troughs in Fig. 10. Fig. 11 shows different perspectives of the full canopy at the five different instants (phases). In phase α , the canopy is fully inflated, while in phase γ both the band and the disk are partially collapsed. The intermediate phase β shows mostly a collapse of the band, suggesting that the disk starts to collapse only after the band is experiencing strong nonlinear instabilities. On the way back to full inflation, phase δ , the band and disk remain partially collapsed. In these figures, the pictures were rescaled to occupy the full area of the image so as to avoid having too small views of the canopy in the collapsed states. The actual change of projected area between phase α and γ is approximately 60%, as indicated previously. For completeness, Fig. 12 shows the canopy configurations at the same phases of the breathing cycle for Case C. Although the Mach number is higher in this case, there are no obvious qualitative differences in the shapes of the canopy.

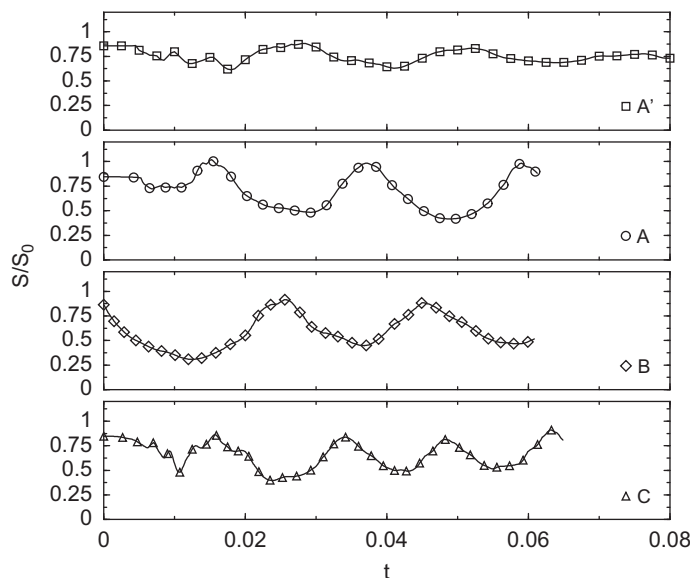


Fig. 9. Projected frontal area of the canopy as a function of time for all cases.

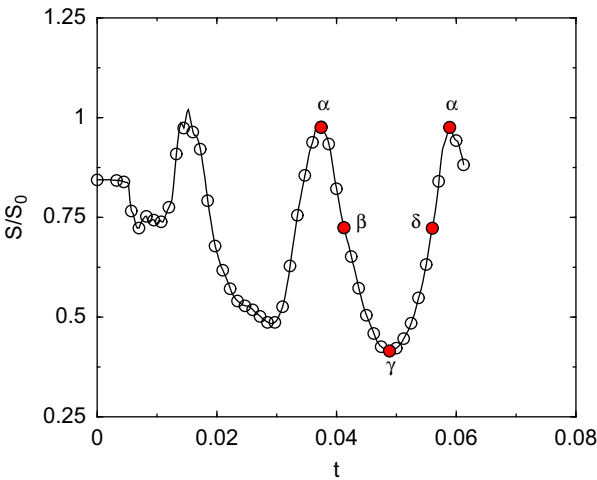


Fig. 10. Projected canopy area for Case A as a function of time with marked instants corresponding to a breathing cycle.

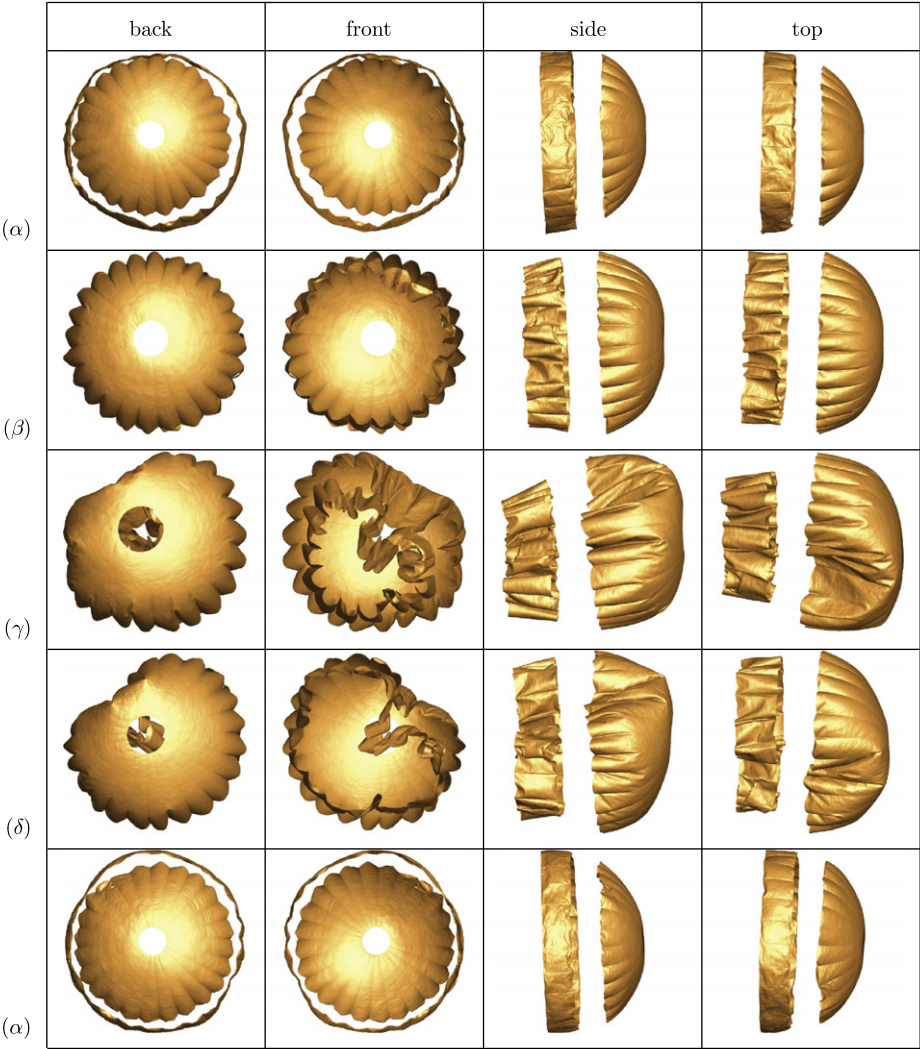


Fig. 11. Four views of the canopy from simulation A in a complete breathing cycle (phases α trough δ).

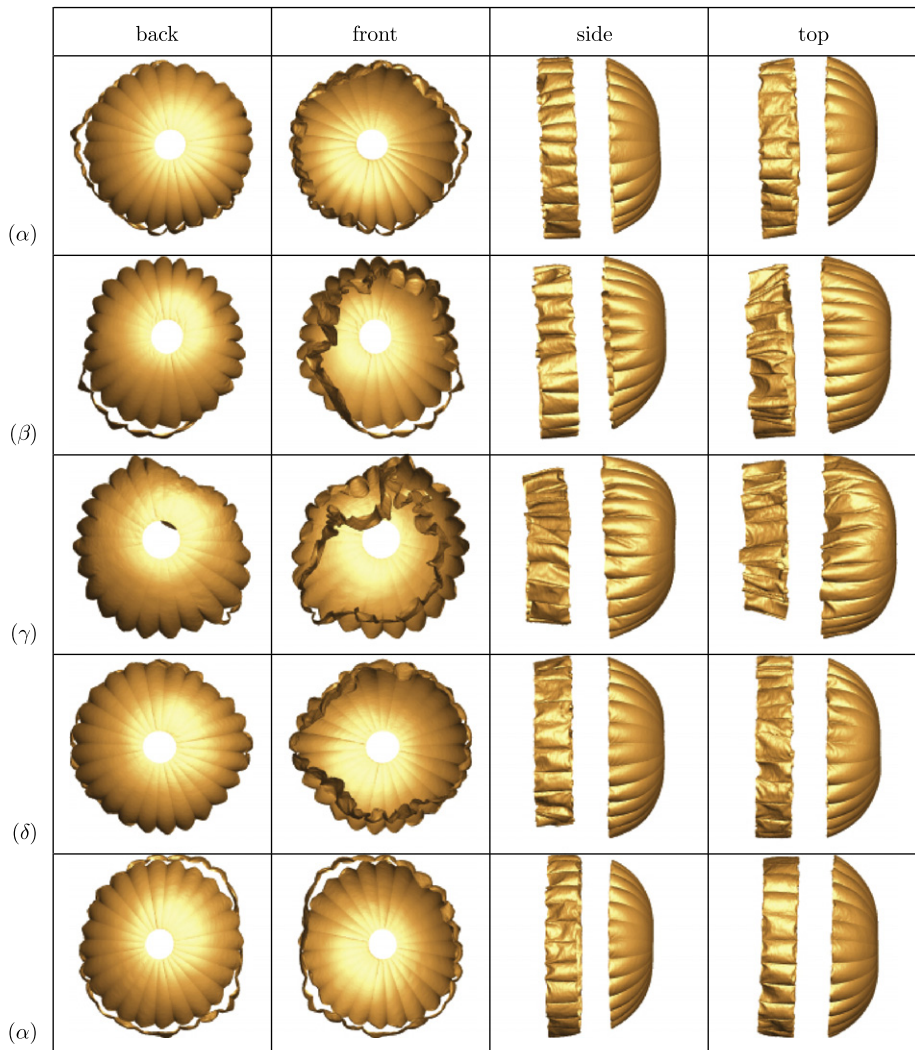


Fig. 12. Four views of the canopy from simulation C in a complete breathing cycle (phases α trough δ).

5.2. Forces

In all cases, the drag on the rigid capsule remains insensitive to the dynamics of the trailing canopy. As discussed previously, the bow shock ahead of the capsule is very stable and it is not easily perturbed by the dynamics of the turbulent wake behind the capsule (although the flow is subsonic in this region). The capsule drag achieves steady state quickly and varies by less than 1% during each simulation. The drag caused by the canopy behaves differently. Fig. 13 shows the corresponding canopy drag history for all cases. The initial period between $t=0$ and 25 ms clearly shows the transient adjustment of the canopy to the supersonic flow initiated by the passage of the shock used to initialize the flow. In this period, the drag shows an intermittent behavior, where the cables are sometimes under tension as the canopy moves upstream and sometimes relaxed (no force transmitted) as the canopy moves downstream. After this initial period, the canopy appears to enter immediately into the breathing cycle that is characteristic of these parachutes. This results in quasi-periodic evolution of the drag in all cases, except A'. The most amplified behavior is observed at the higher Mach number, where the low point in the drag approaches very small values, relatively speaking. The low drag value in the breathing cycle is approximately 1/12 of the peak drag for Case C. This is not as prominent for Cases A and B, which are roughly indistinguishable, with a low drag of approximately 1/5 of their corresponding peaks. The observed performance of the drag in the simulations is consistent with the behavior of these parachutes, which tend to deteriorate dramatically beyond Mach 2.5.

Average drags over one breathing cycle for the capsule, F_c , and the canopy, F_p , and their corresponding drag coefficients are listed in Table 2. Comparison with the experimental values for Cases B and C shows that the simulations indicate values of the drag approximately 10% and 20% lower, respectively. The drag for Case B is within experimental uncertainties and modeling differences between the experimental geometry and the simulation. In particular, the experiment is carried out in a finite

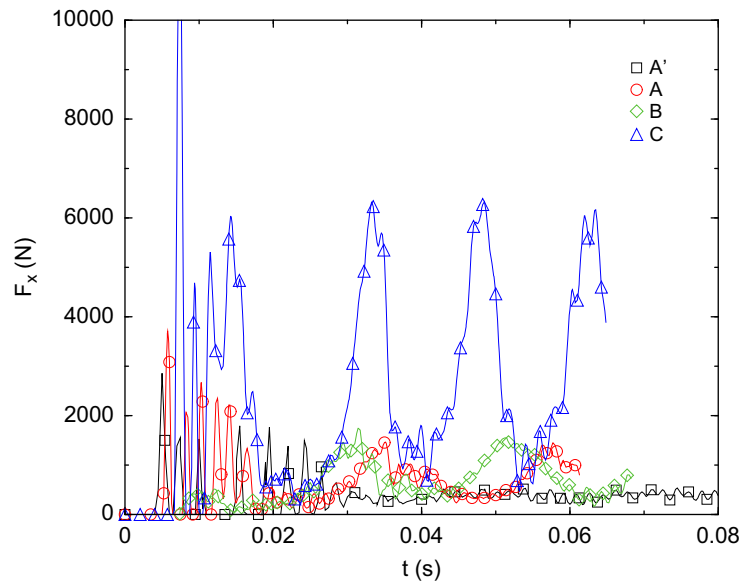


Fig. 13. Drag of the canopy as a function of time for all cases.

Table 2

Forces and drag coefficients of the different simulation cases and experiment (Sengupta et al., 2008).

Case	F_c (N)	F_p (N)	C_c	C_p	C_{exp}
A'	123	388	1.29	0.18	–
A	130	717	1.37	0.34	–
B	130	834	1.37	0.40	0.44
C	606	2796	1.39	0.29	0.38

cross-section wind tunnel, where the walls induce a confinement effect due to the blockage of the parachute system. In our simulations, characteristic boundary conditions are used at the boundaries of the domain and these are more appropriate for a free-flying parachute. In addition, there is no wall-turbulence modeling at the flexible walls of the canopy, which should increase the overall drag. Another effect specific to the parachute is the presence of the suspension lines. As indicated earlier, these cables are not modeled in the simulations because they are too thin for the resolution we can afford. Nevertheless, the photogrammetry in Sengupta et al. (2008) and Sengupta et al. (2009a) clearly shows that there is vent blockage and turbulence-shock boundary layer separation from the cables. The shed turbulent flow completely alters and interferes with the bow shock ahead of the canopy and is probably the most likely explanation of the large difference in drag observed for Case C. In a full-scale parachute, typically with a diameter around 30 m, the relative thickness of the wires with respect to the canopy is much smaller than those used in the experiments referenced above. Therefore, it is expected that the wires will play a lesser role in their contribution to the drag.

The lateral drag caused by the canopy is predicted by the simulations to be a very intermittent function of time. Fig. 14 shows the yaw and pitch pull angle as a function of time from all the simulations. As can be seen, the mean angle fluctuates around 5° for Cases A to C, with additional sharp local fluctuations of approximately 1° . The time step used in the simulations is well within the temporal resolution required for these figures (there are approximately 16 time steps within a single fast period shown in the figure).

5.3. Effect of resolution

As indicated previously, Case A' shows an abnormally low breathing strength. Although it is not possible to completely ascertain if a simulation at even finer resolution than that used in Case A (which we could not afford) will show different dynamics, the favorable qualitative, and to some extent quantitative, comparisons of Cases B and C with experimental results support the initial assessment that the grid size in Cases A to C is appropriate. This cannot be inferred in Case A', since both the forces and the dynamics of the breathing are substantially different. After comparing the flow solutions between simulations A' and A it was observed that the bow shock ahead of the canopy stabilizes in an unphysical location for Case A'. Fig. 15 shows a detail of the center region of the simulation between the turbulent wake of the capsule and the bow shock of the canopy for Cases A' and A. The isocontour colors denote the instantaneous streamwise velocity. We observe that the size of the turbulent

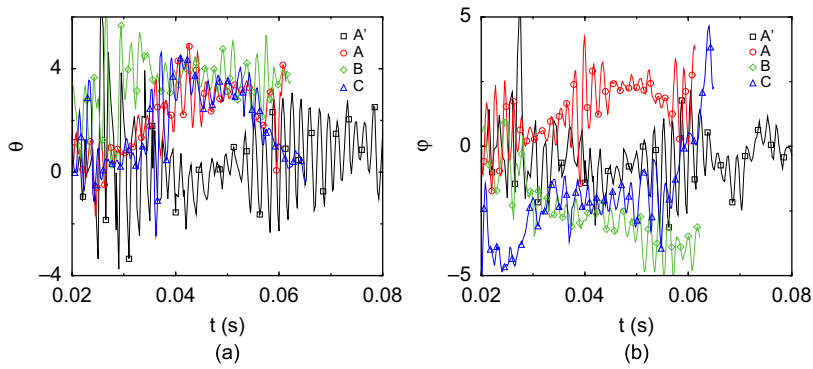


Fig. 14. Yaw and pitch pull angles for all cases as a function of time.

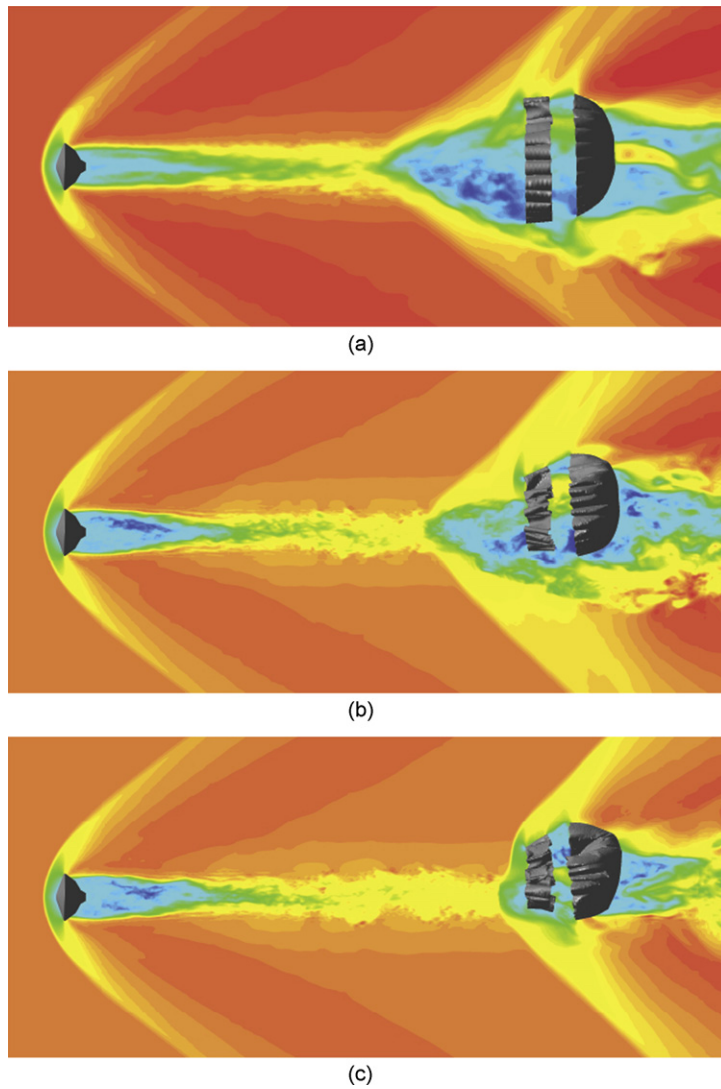


Fig. 15. Streamwise velocity through the center of the domain for Case A' (a) and Case A (b,c) at different instants.

wake core and the strength of the velocity deficit are much larger in Case A', Fig. 15(a), in comparison with that observed in Case A, Figs. 15(b) and (c). The excess in the velocity deficit of the wake prediction of the coarse-resolution simulation is so large that the bow shock does not form ahead of the canopy. We observe, instead, an approximately conical shock (shown as

two oblique shocks in the picture) which are quite stable. In a sense, the wake passes through this region without affecting the compression region and it seems to be a possible explanation as to why the flow is more stable. We also include two different instants in Case A, where the wake displaces the bow shock (b), and one where the wake and the bow shock interact directly (c). Some instances of Case A also show the configuration seen in subfigure (a), with the bow shock adopting a position outside of the turbulent wake, but the bow shock always closes as shown in subfigure (c). An alternative interpretation of these results, is obtained by comparing the Mach number isolevels (not shown). It is observed that there is always a subsonic path in Case A' connecting the capsule with the canopy while this region rarely exists in Case A. We believe that these observations indicate that the resolution for Case A' was inadequate to model the wake–shock interaction. The poor wake resolution resulted in a completely unphysical shock configuration; minimizing the interaction with the canopy.

6. Conclusions

Large-scale fluid–structure simulations of compressible flow over flexible supersonic disk-gap-band parachutes were performed and compared with experimental results of NASA at matching conditions and structural properties. The computational model employed adaptive mesh refinement, large-eddy simulation of compressible flows coupled with a thin-shell structural finite-element model. The simulations reproduce the large canopy-area oscillations that are usually observed in these systems around and above Mach 2. The calculated drag compared favorably with the measured values, with decreasing mean and increasing variability of the drag with increasing Mach number. The largest difference with the experiments was obtained for the highest Mach numbers, approximately 20% difference, which is attributed to limitations in the modeling of the suspension lines of the canopy and the simplifications introduced as part of the modeling of the unsteady, deformable, turbulent boundary layers present in this configuration. Finally, it was observed that the canopy-area oscillations were only observed when the resolution of the simulation was fine enough, with a coarse simulation practically lacking in this important dynamic behavior due to poor turbulence resolution.

Acknowledgments

This work was supported by the Jet Propulsion Laboratory under Contract 1291711 with the California Institute of Technology (technical program manager Dr A. Sengupta). The authors would like to thank Prof. P.E. Dimotakis for introducing them to the flow-physics of supersonic parachutes. The authors are also thankful to the Supercomputing and Visualization Facility of the Jet Propulsion Laboratory for providing the computational time used for the simulations.

References

- Babish III, C., 1966. Drag let-L staging through modification of supersonic wake views by trailing aerodynamic decelerators. In: AIAA Aerodynamic Deceleration Systems Conference, No. AIAA-1966-1506.
- Barnhardt, M., Drayna, T., Nompelis, I., Candler, G., Garrard, W., 2007. Detached eddy simulations of the MSL parachute at supersonic conditions. In: 19th AIAA Aerodynamic Decelerator Technology Conference and Seminar, Williamsburg, VA, USA.
- Bastianon, R., 1968. Steady and un-steady solution of the flow field over concave bodies in a supersonic free stream. In: Third AIAA Aerodynamic Systems Technology Conference, No. AIAA-1968-946.
- Bendura, R., Huckins III, E., 1968. Performance of a 19.7-meter-diameter disk-gap-band parachute in a simulated Martian environment. Technical Report X-1499, NASA, Washington, D.C., USA.
- Bendura, R., Lundstrom, R., Renfro, P., Lecroy, S., 1974. Flight tests of Viking parachute system in three Mach number regimes. 2: parachute test results. Technical Report TN-D7734, NASA, Washington, D.C., USA.
- Charczenko, N., 1962. Parachute performance at supersonic speeds. In: Meeting on Space Vehicle and Landing and Recovery Research and Technology, Washington, DC, USA.
- Charczenko, N., 1964. Wind-tunnel investigation of drag and stability of parachutes at supersonic speeds. Technical Report X-991, NASA, Washington, D.C., USA.
- Cirak, F., Deiterding, R., Mauch, S., 2006. Large-scale fluid–structure interaction simulation of viscoplastic and fracturing thin shells subjected to shocks and detonations. *Computers and Structures* 85 (11–14), 1049–1065.
- Cirak, F., Ortiz, M., 2001. Fully C^1 -conforming subdivision shell elements for finite deformation thin-shell analysis. *International Journal of Numerical Methods in Engineering* 51 (7), 813–833.
- Cirak, F., Ortiz, M., Schröder, P., 2000. Subdivision surfaces: a new paradigm for thin-shell time-element analysis. *International Journal of Numerical Methods in Engineering* 47 (12), 2039–2072.
- Couch, L., 1975. Drag and stability characteristics of a variety of reefed and unreefed parachute configurations at Mach 1.80 with an empirical correlation for supersonic Mach numbers. Technical Report TR-R429, NASA Langley Research Center.
- Cruz, J., Kandis, M., Witkowski, A., 2003a. Opening loads analyses for various disk-gap-band parachutes. In: 17th AIAA Aerodynamic Decelerator Systems Technology Conference and Seminar, No. AIAA-2003-2131, Monterey, CA, USA.
- Cruz, J., Mineck, R., Keller, D., Bobskill, M., 2003b. Wind tunnel testing of various disk-gap-band parachutes. In: 17th AIAA Aerodynamic Decelerator Systems Technology Conference and Seminar, No. AIAA-2003-2129, Monterey, CA, USA.
- Davenport, E., 1969. Static longitudinal aerodynamic characteristics of some supersonic decelerator models at Mach numbers of 2.30 and 4.63. Technical Report TN D-5219, NASA, Washington, D.C., USA.
- Deiterding, R., Radovitzky, R., Mauch, S., Noels, L., Cummings, J., Meiron, D., 2006. A virtual test facility for the efficient simulation of solid materials under high-energy shock-wave loading. *Engineering with Computers* 22 (3–4), 325–347.
- Eckstrom, C., 1966. Development and testing of the disk-gap-band parachute used for low dynamic pressure applications at ejection altitudes at or above 200,000 feet. Technical Report CR-502, NASA.
- Eckstrom, C., 1970. Flight test of a 40-foot-nominal-diameter disk-gap-band parachute deployed at a Mach number of 3.31 and a dynamic pressure of 10.6 pounds per square foot. Technical Report TM X-1924, NASA, Washington, D.C., USA.

- Eckstrom, C., Preisser, J., 1967. Flight test of a 30-foot-nominal-diameter disk-gap-band parachute deployed at a Mach number of 1.56 and a dynamic pressure of 11.4 pounds per square foot. Technical Report TM X-1451, NASA.
- Fedkiw, R., Aslam, T., Merriman, B., Osher, S., 1999. A non-oscillatory Eulerian approach to interfaces in multimaterial flows (the ghost fluid method). *Journal of Computational Physics* 152 (2), 457–492.
- Geurts, B., 2008. Regularization modeling for LES of separated boundary layer flow. *Journal of Fluids and Structures* 24 (8), 1176–1184.
- Gidzak, V., Barnhardt, M., Drayna, T., Nompelis, I., Candler, G., Garrard, W., 2009. Comparison of fluid–structure interaction simulations of the MSL parachute with wind tunnel tests. In: 20th AIAA Aerodynamic Decelerator Systems Technology Conference and Seminar, Seattle, WA, USA.
- Gillis, C., 1973. The Viking decelerator system—an overview. In: Fourth AIAA Aerodynamic Deceleration Systems Conference, Palms Springs, California.
- Gillis, C., Bendura, R., 1968. Full-scale simulation of parachute deployment environment in the atmosphere of Mars. In: 14th Annual Technical Meeting of the Institute of Environmental Sciences, St. Louis, Missouri, USA.
- Heinrich, H., 1966. Aerodynamics of the supersonic guide surface parachute. *Journal of Aircraft* 3 (2), 105–111.
- Houmard, J., 1973. Stress analysis of the Viking parachute. In: Fourth AIAA Aerodynamic Decelerator Systems Conference, Palm Springs, CA, USA.
- Houtz, N., 1964. Optimization of inflatable drag devices by isotosoid design. In: First AIAA Annual Meeting, Washington, D.C., pp. 64–75.
- Johari, H., Levshin, A., 2009. Interaction of a line vortex with a round parachute canopy. *Journal of Fluids and Structures* 25 (8), 1258–1271.
- Johnson, C., 1960. Investigation of the characteristics of 6-foot drogue-stabilization ribbon parachutes at high altitudes and low supersonic speeds. Technical Report X-448, NASA, Washington, D.C., USA.
- Kosovic, B., Pullin, D.I., Samtaney, R., 2002. Subgrid-scale modeling for large-eddy simulations of compressible turbulence. *Physics of Fluids* 14, 1511–1522.
- Lafarge, R., Nelsen, J., Gwinn, K., 1994. A novel CFD/structural analysis of a cross parachute. In: 32nd AIAA Aerospace Sciences Meeting and Exhibit, No. AIAA-1994-752.
- Lemke, R., 1967. Final report on the 40 ft DBG parachute. Technical Report CR-66587, NASA, Martin Marietta Corporation, Denver, Colorado, USA.
- Lesieur, M., Metais, O., 1996. New trends in large-eddy simulations of turbulence. *Annual Reviews of Fluid Mechanics* 28, 45–82.
- Lingard, J., Darley, M., 2005. Simulation of parachute fluid structure interaction in supersonic flow. In: 18th AIAA Aerodynamic Decelerator Systems Technology Conference and Seminar, No. AIAA-2005-1607, Munich, Germany.
- Lingard, J., Darley, M., Underwood, J., 2007. Simulation of Mars supersonic parachute performance and dynamics. In: 19th AIAA Aerodynamic Decelerator Technology Conference and Seminar, No. AIAA-2007-2507, Williamsburg, VA, USA.
- Lombardini, M., 2008. Richtmyer–Meshkov instability in converging geometries. Ph.D. Thesis, California Institute of Technology.
- Lundgren, T.S., 1982. Strained spiral vortex model for turbulent fine-structure. *Physics of Fluids* 25, 2193–2203.
- Lundstrom, R., Raper, J., Bendura, R., Shields, E., 1974. Flight tests of Viking parachute system in three Mach number regimes. Vehicle description, test operations, and performance. Technical Report TN-D7692, NASA, Washington, D.C., USA.
- Maydew, R., Peterson, C., 1991. Design and testing of high-performance parachutes. Technical Report AG-319, AGARD.
- Mayhue, R., Bobbitt, P., 1972. Drag characteristics of a disk-gap-band parachute with a nominal diameter of 1.65 meters at Mach numbers from 2.0 to 3.0. Technical Report TN D-6894, NASA, Washington, D.C., USA.
- Maynard, J., 1960. Aerodynamics of decelerators at supersonic speeds. In: AIAA Proceedings of the Recovery of Space Vehicles Symposium, pp. 48–54.
- Maynard, J., 1961. Aerodynamic characteristics of parachutes at Mach numbers from 1.6 to 3. Technical Report D-752, NASA, Washington, D.C., USA.
- Mikulas, M., Bohon, H., 1968. Summary of the development status of attached inflatable decelerators. In: Third AIAA Aerodynamic Systems Technology Conference.
- Misra, A., Pullin, D.I., 1997. A vortex-based subgrid stress model for large-eddy simulation. *Physics of Fluids* 9, 2443–2454.
- Moog, R., Bendura, R., Timmons, J., Lau, R., 1974. Qualification flight tests of the Viking decelerator system. *Journal of Spacecraft* 11 (3), 188–195.
- Mosler, J., Cirak, F., 2009. A variational formulation for finite deformation wrinkling analysis of inelastic membranes. *Computer Methods in Applied Mechanics and Engineering* 198, 2087–2098.
- Murrow, H., Henke, D., Eckstrom, C., 1973. Development flight tests of the Viking decelerator system. In: Fourth AIAA Aerodynamic Deceleration Systems Conference, Palms Springs, CA, USA.
- Nelsen, J., 1995. Computational fluid dynamic studies of a solid and ribbon 12-gore parachute canopy in subsonic and supersonic flow. In: 13th AIAA Aerodynamic Decelerator Systems Technology Conference, No. AIAA-95-1558.
- Nerem, R., Pake, F., 1973. A model and calculation procedure for predicting parachute inflation. In: Fourth AIAA Aerodynamic Deceleration Systems Conference, Palm Springs, CA, USA.
- Nickel, W., Sims, L., 1964. Study and exploratory free-flight investigation of deployable aerodynamic decelerators operating at high altitudes and at high Mach numbers. Technical Report FDL-TDR-64-35, US Air Force.
- Peterson, C., Strickland, J., 1996. The fluid dynamics of parachute inflation. *Annual Reviews of Fluid Mechanics* 28, 361–387.
- Pinnell, W., Bloetscher, F., 1966. Correlation of analytical and empirical techniques for designing supersonic and hypersonic decelerators. In: AIAA Aerodynamic deceleration systems conference, No. AIAA-1966-1517.
- Pipkin, C., 1994. Relaxed energy densities for large deformation of membranes. *IMA Journal of Applied Mathematics* 52, 297–308.
- Poole, L., 1972. Effects of suspension-line damping on LADT #3 and supersonic bldt parachute inflation dynamics. Technical Report LWP-1050, NASA Langley Research Center.
- Pope, S.B., 2004. Ten questions concerning the large-eddy simulation of turbulent flows. *New Journal of Physics* 6, Art. 35.
- Pullin, D.I., 2000. A vortex-based model for the subgrid flux of a passive scalar. *Physics of Fluids* 12, 2311–2319.
- Queen, E., Raiszadeh, B., 2002. Mars smart lander parachute simulation model. In: AIAA Atmospheric flight mechanics conference and exhibit, No. AIAA-2002-4617, Monterey, CA, USA.
- Reuter, J., Machalick, W., Witkowski, A., Kandis, M., Sengupta, A., Kelsch, R., 2009. Design of subscale parachute models for MSL supersonic wind tunnel testing. In: 20th AIAA Aerodynamic Decelerator Systems Technology Conference and Seminar, No. 2999-569, Seattle, WA, USA.
- Ross, R., Nebiker, F., 1966. Survey of aerodynamic deceleration systems. In: Third AIAA Annual Meeting, No. 66-988, Boston, MA, USA.
- Sengupta, A., Kelsch, R., Roeder, J., Wernet, M., Witkowski, A., Kandis, M., 2009a. Supersonic performance of disk-gap-band parachutes constrained to a 0-degree trim angle. *Journal of Spacecraft and Rockets* 46 (6), 1155–1163.
- Sengupta, A., Roeder, J., Kelsch, R., Wernet, M., Kandis, M., Witkowski, A., 2008. Supersonic disk gap band parachute performance in the wake of a Viking-type entry vehicle from Mach 2 to 2.5. In: AIAA Atmospheric flight mechanics conference and exhibit, No. AIAA-2008-6217, Honolulu, Hawaii.
- Sengupta, A., Steltzner, A., Witkowski, A., Candler, G., Pantano, C., 2009b. Findings from the supersonic qualification program of the Mars Science Laboratory parachute system. In: 20th AIAA Aerodynamic Decelerator Systems Technology Conference and Seminar, No. AIAA 2009-2900, Seattle, WA, USA.
- Sengupta, A., Wernet, M., Roeder, J., Kelsch, R., Witkowski, A., Jones, T., 2009c. Supersonic testing of 0.8 m disk gap band parachutes in the wake of a 70 deg sphere cone entry vehicle. In: 20th AIAA Aerodynamic Decelerator Systems Technology Conference and Seminar, Seattle, WA, USA.
- Silbert, M., 1983. Deployment of a spin parachute in the altitude region of 260,00 ft. *Journal of Spacecraft and Rockets* 20 (1), 11–14.
- Silbert, M., Gilbertson, G., 1989. High altitude decelerator systems. In: 10th AIAA Aerodynamic Decelerator Systems Technology Conference, Cocoa Beach, FL, USA.
- Simo, J.C., Fox, D.D., 1989. On a stress resultant geometrically exact shell model. Part i: formulation and optimal parametrization. *Computer Methods in Applied Mechanics and Engineering* 72, 267–304.
- Steinberg, S., Siemers III, P., Slayman, R., 1974. Development of the Viking parachute configuration by wind-tunnel investigation. *Journal of Spacecraft* 11 (2), 101–107.
- Stevens, G., 1972. A theory of vibrations in parachutes. *Journal of Aircraft* 9 (1), 74–78.
- Strickland, J., Macha, J., 1990. Preliminary characterization of parachute wake recontact. *Journal of Aircraft* 27 (6), 501–506.

- Taylor, A., Tutt, B., Sanders, J., 2003. On the application of explicit finite element analysis and coupled fluid/structure simulations as they apply to escape and recovery systems. In: 41st Annual survival and flight equipment association symposium, Jacksonville, Florida, pp. 78–87.
- Taylor, G.I., 1963. On the shapes of parachutes. In: *The Scientific Papers of G.I. Taylor*. Cambridge University Press.
- Voelkl, T., Pullin, D.I., Chan, D.C., 2000. A physical-space version of the stretched-vortex subgrid-stress model for large-eddy simulation. *Physics of Fluids* 12, 1810–1825.
- Wagner, H., 1929. Flat sheet metal girders with very thin metal web. Part I: General theories and assumptions. *Zeitschrift für Flugtechnik und Motorluftschiffahrt* 20 (8), 200–207.
- Whitham, G., 1999. *Linear and Nonlinear Waves*. Wiley-Interscience, New York.
- Whitlock, C., Bendura, R., 1969. Inflation and performance of three parachute configurations from supersonic flight test in a low-density environment. Technical Report TN D-5296, NASA, Washington, D.C., USA.
- Whitlock, C., Bendura, R., Coltrane, L., 1967. Performance of a 26-meter-diameter ringsail parachute in a simulated Martian environment. Technical Report TM X-1356, NASA, Washington, D.C., USA.
- Zang, T.A., Dahlburg, R.B., Dahlburg, J.P., 1992. Direct and large-eddy simulations of 3-dimensional compressible Navier–Stokes turbulence. *Physics of Fluids A—Fluid Dynamics* 4, 127–140.